ACS OMEGA

http://pubs.acs.org/journal/acsodf

Article

Ni–Fe/Reduced Graphene Oxide Nanocomposites for Hexavalent Chromium Reduction in an Aqueous Environment

Zeyu Kang, Hui Gao,* Zhongliang Hu, Xiaodong Jia, and Dongsheng Wen*

Cite This: *ACS Omega* 2022, 7, 4041−4051

Read Online

ACCESS | Metrics & More | Article Recommendations | Supporting Information

ABSTRACT: We designed and synthesized a novel high efficiency Cr(VI) removal material using reduced graphene oxide (RGO) as a support with high specific surface area and a mixture of Fe and Ni nanoparticles (NPs) as a catalytic reducing agent. Such a design enables the composite particle to be integrated with three functions of adsorption, catalysis, and reduction, where RGO could enhance Cr(VI) adsorption, while Fe/Ni NPs increase the catalytic reducing efficiency. The application of a microchip mixer guaranteed a better mixing of GO and subsequent decoration of Fe and Ni NPs on RGO. Cr(VI) removal experiments with various materials are performed, and the results demonstrated that the Ni–Fe/RGO achieved an adsorption capacity of 150.45 mg/g at pH = 7 and 197.43 mg/g at pH = 5 for Cr(VI), which is higher than those of other reported materials at a pH of ∼7. To the best of our knowledge, this is the first example of Ni–Fe/RGO for efficient Cr(VI) removal by using the synergistic effects of increased adsorption, catalysis-assisted reduction, and enhanced mixing effect of a microchip mixer. This work also provides us with a simple and low-cost method for the fabrication of an effective Cr(VI) removal material.

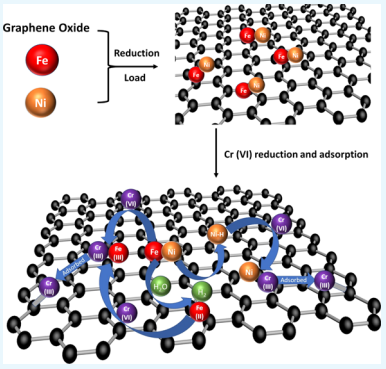

1. INTRODUCTION

General increase of waste gas, water, and soil with the intensification of human activities has resulted in serious environmental problems, which in turn cause severe threats to humans.[1] Among those, heavy metal pollution has raised widespread attention due to its bioaccumulation and non-degradability.[2,3] Chromium (Cr) is one typical heavy metal contaminant, which is widely present in the environment because it is extensively used in many industrial processes such as metallurgical industry, chemical industry, refractory, and cast iron.[4] Chromium exists in the environment, mainly in the stable state of trivalent chromium [Cr(III)] and hexavalent chromium [Cr(VI)]. Cr(III) is an essential element for the human body, and its toxicity is relatively low. However, the toxicity of Cr(VI) is about 100 times that of Cr(III),[5] showing much higher environmental and health risks. It could penetrate the human circulation system via drinking water or enrichment by the food chain and bring some detrimental effects to humans.

To solve the above mentioned problem, a lot of advanced treatment technologies have been applied for efficient Cr(VI) removal and remediation, such as chemical precipitation,[6] ion exchange,[7] adsorption, membrane filtration, flotation,[8] and electrochemical treatment.[9] Among them, chemical precipitation is by far the most widely used process for industrial wastewater processing,[10] owing to that it is cost-effective and straightforward to operate. As an active metal with a standard redox potential (E_0 = −0.44 V), zero-valent iron (ZVI) has been proposed as a chemical precipitation agent to remove chromium contaminants.[11−14] For example, Cr(VI) could be reduced by ZVI and form insoluble precipitates $Cr(OH)_3$ with much lower toxicity in a neutral or alkaline environment. Notably, ZVI is nontoxic, inexpensive, and easy to produce, which is good for large-scale applications in the industry. Hence, different types of ZVI materials have been used for the removal of chromium contaminants, including conventional micrometer-sized ZVI and nanometer-sized ZVI (NZVI).

For the evaluation of the chromium removal ability of different ZVI materials, Cr(VI) adsorption capacity (mg/g) is used to assess their performance. Previous studies demonstrated that the environmental pH matters the ZVI's adsorption capacity of Cr(VI).[15−17] Because the main Cr(VI) species in water are $Cr_2O_7^{2}$ and $HCrO_4^{-}$ at low pH and CrO_4^{2-} at high pH,[18] respectively. The electrostatic force and competition between OH^- and precipitation agents will lead to a lower Cr(VI) adsorption capacity at a higher pH.[19] Hence, the pH value must be considered when comparing Cr(VI) adsorption capacity. Conventional micrometer-sized ZVI presents the ability of Cr(VI) removal, but a relatively low adsorption capacity limits its application.[20] In contrast, with a much higher specific surface area, NZVI shows a better Cr(VI) removal potential.[15−17] Montesinos et al.[21] used bare NZVI to

Received: September 22, 2021
Accepted: January 19, 2022
Published: January 28, 2022

remove Cr(VI) and obtained an adsorption capacity of 47.2 ± 0.1 mg/g at pH = 5 and 411 ± 24 mg/g at pH = 3, respectively. The adsorption capacity of 60.03 mg/g at pH = 6.8 was found by Chen et al.[22] and 10.06 mg/g at pH = 6.36 by Ai et al.[23]

These studies demonstrated NZVI's great potential as a Cr removal agent; however, using pure NZVI still has its disadvantages. It is poor in stability as a highly active material and may react with surrounding media during the preparation and storage process.[24] The presence of large specific surface area makes them prone to aggregate[25] and then led to blocking troubles in water treatment, which will decrease the adsorption capacity and produce secondary pollution.[26] Besides, the separation of NZVI from the treated solution also presents a big challenge. Some researchers tried to solve these problems through dispersion methods but did not get distinct improvement for Cr species adsorption capacity. Zhou et al.[27] tried to use an ultrasonic device to optimize NZVI dispersion property, and finally achieved an adsorption capacity of 66.7 mg/g at pH = 5.5. Lv et al.[28] employed a mixture of NZVI-Fe_3O_4 dispersion and enabled an adsorption capacity of 29.43 mg/g at pH = 8. This very much limits the choice and application of pure NZVI as a tool to remove Cr species.

In order to solve the problem and increase Cr(VI) adsorption capacity, a series of new NZVI-based materials have been investigated,[29−37] which can be classified into two types: bimetal materials and sorbent-supported materials. For bimetal materials, iron is used as the primary metal, and a transition metal such as palladium (Pd),[29] copper (Cu),[30] nickel (Ni), or cerium (Ce) is used as another reduction or catalytic material. For example, Chen et al.[31] composited Fe−Ce bimetal oxide and obtained a maximum adsorption capacity of 75.36 mg/g at pH = 4. Wen et al.[32] reported a Fe−Ce bimetal oxide with an adsorption capacity of 125.28 mg/g at pH = 3. Fe−Ni bimetal synthesized in an ultrasound-assisted system was proposed by Zhou et al.[33] and demonstrated with an adsorption capacity of 67.6 mg/g at pH = 5. Such bimetal material systems show better effects than that of the pure NZVI system at similar pH conditions.[38] Despite the bimetal material having great advantages compared to the pure NZVI system, there are some limitations for bimetal materials. (I) As a powdered material, it tends to aggregate together, which hugely affects the adsorption capacity. (II) The bimetal metal material can only reduce heavy metal to a lower valence state, such as Cr(VI) to Cr(III). The Cr(III) is not immobilized, and it can continue to diffuse in the environment to generate secondary pollution. (III) The NPs are hard to collect back in practical application, which will increase the operating costs.

For sorbent supporting materials, the composites combine both functions of reduction by NZVI and enhanced adsorption by other materials to remove Cr(VI) from water. A series of adsorbent materials were employed to support NZVI and investigated in detail. Shi et al.[34] synthesized bentonite-supported NZVI and obtained an adsorption capacity of 7.3 mg/g at pH = 6. Fu et al.[35] prepared sepiolite-supported NZVI and got a better adsorption capacity of 43.86 mg/g at pH = 6. Wang et al.[36] composited carboxymethyl cellulose-supported NZVI and demonstrated its adsorption capacity of 33 mg/g at pH = 5.5. Sharma et al.[37] studied cellulose-supported NZVI at pH = 3, showing an adsorption capacity of 562.8 mg/g; they found that, however, the exceptionally high adsorption capacity was mainly contributed by the low pH environment.

Reduced graphene oxide (RGO) is a recently developed adsorbent with a two-dimensional single atomic layer structure, which possesses an extremely high specific surface area.[39] It has been reported that higher Cr(VI) adsorption capacity can be obtained when using a graphene-related material as a base supporting material, such as RGO and graphene oxide (GO). Jabeen et al.[40] synthesized graphene-NZVI and got an adsorption capacity of 162 mg/g at pH = 4.25. Li et al.[41] found that graphene-NZVI's adsorption capacity can reach 180.16 mg/g at pH = 5. Li et al.[42] confirmed an adsorption capacity of 21.72 mg/g at pH = 7 for graphene-supported NZVI. Lv et al.[43] decorated NZVI on magnetic Fe_3O_4/graphene and observed an adsorption capacity of 66.22 mg/g at pH = 8. Wang et al.[44] loaded Fe_3O_4 on PEI-modified GO and found that its adsorption capacity can change from around 250 to 50 mg/g when tuning pH from 2 to 7. In addition, there have been some attempts to combine the advantages of bimetal and sorption materials, but the results were not satisfactory. Lu et al.[45] showed that by using the Fe−Ni bimetal-decorated montmorillonite, the adsorption capacity is only about 65 mg/g at pH = 3. This might be due to the relatively low surface area (77.7 m^2/g), which is limited by the base material montmorillonite. Replacing the base supporting material to that with a higher BET surface area may be effective and useful. Although sorbent supporting materials overcome some disadvantages of the bimetal material, most of sorbent supporting materials with excellent selectivity is relatively complex and needs more research studies on industry application.

In this work, we developed a new strategy of producing highly efficient Cr(VI) removal material by combining three functions (i.e., adsorption, catalysis, and reduction) into one: RGO is used to increase the specific surface area to enhance the adsorption of Cr(VI); a mixture of Fe and Ni NPs is applied to increase the catalytic reducing efficiency, and a microchip mixer is utilized to better mix and decorate Fe and Ni NPs on the RGO. A series of Cr(VI) removal experiments are carried out and investigated their performance in detail. The results demonstrated that a high adsorption capacity for Cr(VI) of such novel material can be achieved at pH = 7.

2. EXPERIMENTAL SECTION

2.1. Materials and Instruments. *2.1.1. Materials.* GO is synthesized by a modified Hummer's method using graphite powder as a raw material. $FeCl_3{\cdot}6H_2O$ and potassium dichromate ($K_2Cr_4O_7$) were bought from SLS (Scientific Laboratory Supplies), and nickel powder (APS 2.2−3.0 μm), polyvinyl pyrrolidone (PVP), and chromium(III) chloride hexahydrate ($CrCl_3$) were purchased from Alfa Aesar. Sodium borohydride ($NaBH_4$) was bought from Fisher Scientific Ltd. 1,5-Diphenylcarbazide (DPC) was purchased from Sigma-Aldrich. The chemicals are used as received without further purification.

2.1.2. Instruments. Scanning electron microscopy (SEM, SU8230, Hitachi) equipped with energy-dispersive X-ray spectroscopy (EDS) is used to measure the sample's morphology and elemental information. Transmission electron microscopy (TEM, FEI Tecnai TF20) is used to observe the RGO sheet structure and Fe−Ni bimetal NP-loaded situation. Fourier-transform infrared (FTIR) spectroscopy experiments are performed with a Thermo Scientific Nicolet iS10 FTIR spectrometer (Thermo Scientific). BET surface areas are tested on Tristar 3000 (Micromeritics). Ultraviolet−visible spectros-

https://doi.org/10.1021/acsomega.1c05273
ACS Omega 2022, 7, 4041−4051

Table 1. Detailed Reaction Conditions of Different Samples

sample no.	30 wt % $FeCl_3·6H_2O$ (g)	GO (g)	Ni (mg)	PVP (g)	$NaBH_4$ (g)	micromixer (yes/no)
sample 1	0.66	0.04			0.75	no
sample 2	0.66	0.04		1.00	0.75	no
sample 3	0.66	0.04	21.58	1.00	0.75	no
sample 4	0.66	0.04		1.00	0.75	yes
sample 5	0.66	0.04	21.58	1.00	0.75	yes

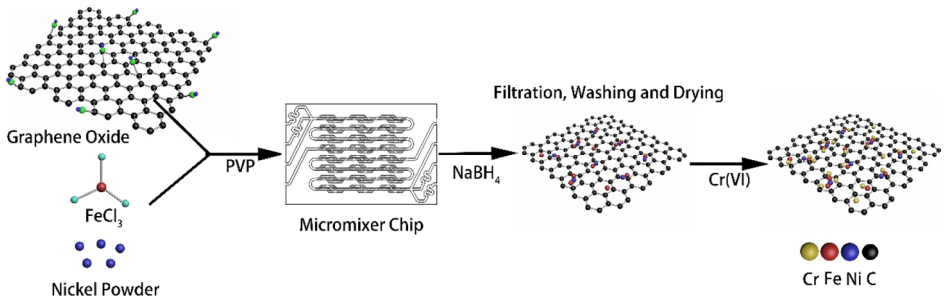

Figure 1. Schematic illustration of the preparation process of the Fe−Ni/RGO composite and its adsorption/reduction of Cr(VI).

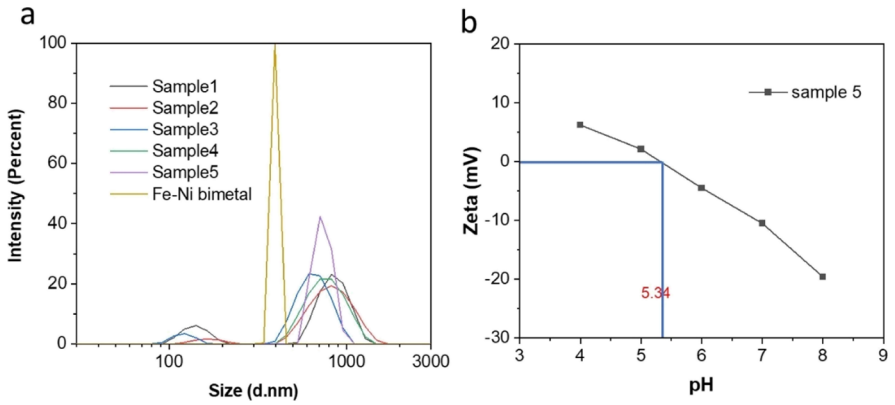

Figure 2. (a) Particle size distribution measured by DLS and (b) zeta potentials of sample 5.

copy (UV−vis) spectra of samples are recorded with a UV spectrophotometer UV-1800 (Shimadzu). Sample size characterization is investigated by dynamic light scattering (DLS) measurements using the Zetasizer Nano ZS (Malvern). HAXPES UHV-XPS is used to confirm the existence and the valence states of elements.

2.2. Preparation of ZVI-NPS, Fe/RGO, and Fe−Ni/RGO Composites. 0.66 g of 30 wt % $FeCl_3·6H_2O$ solution is added into 50 mL of deionized water under magnetic stirring, forming $FeCl_3$ solution. 0.04 g of GO and 1.0 g of PVP are added into the obtained $FeCl_3$ solution and stirred for 30 min. Then, 21.58 mg of nano-nickel powder is added and stirred overnight. The nickel powder shall be surface oxidized by the oxygen in the water. After that, 40 mL of 18.75 mg/mL $NaBH_4$ is added dropwise into the system and stirred overnight. $NaBH_4$ worked as a reducing agent and is expected to reduce Fe^{3+}, GO, and nickel oxide to Fe NPs, RGO, and Ni NPs, respectively. The RGO is used as the base material to support the Fe/Ni bimetal. As H_2 is produced during this step, careful control is needed. The reaction equation is listed below

$$Fe(H_2O)_6^{3+} + 3BH_4^- + 3H_2O = Fe^0 \downarrow + 3B(OH)_3 + 10.5H_2\uparrow$$

For some samples, a micromixer chip (part number 3200401, Dolomite Centre Ltd) is used to replace the magnetic stirring to enhance the mixing and dispersion of GO, Fe, and Ni. The schematic diagram of the micromixer chip is shown in Figure S1 (Supporting Information). The final product is collected by vacuum filtration, washed with ethanol three times, dried in a vacuum oven overnight, and then collected and stored with nitrogen protection. A total of five samples are prepared for the purpose of comparison, as given in Table 1.

3. RESULTS AND DISCUSSION

3.1. Particle Stability, Size, Morphology, and Elemental Analyses. *3.1.1. Influence of Mixing Approach on Composite Particle Stability.* Fe−Ni/RGO composites with the ability to absorb/reduce Cr(VI) are synthesized as shown in Figure 1. Different mixing methods are utilized in this study to prepare samples, that is, magnetic stirring and micromixer chip. The sample solutions obtained by different approaches show different colors and diaphaneity, as shown in Figure S2 (Supporting Information). The solution mixed by the microchip shows high diaphaneity with yellow color, which means that the GO is dispersed very well. In contrast, the solution processed by magnetic stirring presents an opaque

https://doi.org/10.1021/acsomega.1c05273
ACS Omega 2022, 7, 4041−4051

color, indicating the instability and the presence of large GO agglomeration.

3.1.2. Particle Size Analysis. To determine particle size distribution, 15 mg of the sample solution is added into 50 mL of deionized water under sufficient stirring, and a centrifuge is used to separate the sediments and liquid. The upper liquid is tested by Zetasizer, Malvern. As a comparison, the Fe−Ni bimetal is also tested under the same condition. Results are shown in Figure 2 and Table 2. Samples 1−3 show two peaks.

Table 2. Size Distribution Determined by the Intensity

	peak 1		peak 2	
	size (*d*. nm)	% intensity	size (*d*. nm)	% intensity
sample 1	858.0	81.3	141.7	18.7
sample 2	840.7	94.7	166.9	5.3
sample 3	663.2	91.4	120.9	8.6
sample 4	783.4	100		
sample 5	737.0	100		
Fe−Ni bimetal	395.9	100		

It is due to the magnetic stirring process, which could not disperse GO sheets well and some of them became agglomerated. Some Ni or Fe NPs are not fixed onto the RGO surface, resulting in the presence of the second peak around 150 nm. For the Fe−Ni bimetal material without RGO, the aggregation results in the presence of the peak around 400 nm.

As a comparison, samples 4 and 5 produced by the microchannel mixing show only one distribution peak, which means a nonpresence of loose and free Ni and Fe NPs in the system. Because GO is well dispersed in solution and may provide enough points for Ni and Fe NPs to fix on, promoting the formation of an integral three-in-one composite. The results demonstrated that the microchip has a much better mixing and dispersing effect, so as to enable the prepared samples with better properties. For sample 5, the zeta potential decreases from 6.24 to −19.60 mV, and the pHZPC value is 5.34 mV.

3.1.3. Morphology and Elemental Analyses. The morphology and structure of the NZVI/RGO are observed by SEM and TEM, respectively. Figure 3a shows that sample 5 is unordered stacking with a two-dimensional sheet structure; the size of the sheet is about 1 μm, which is in good agreement with the DLS result. The thickness of the sheet is less than 50 nm. The TEM images in Figure 3c show the RGO sheet has a length of the side of about 1 μm, which is well consistent with the SEM results. It also revealed that Fe−Ni NPs are well loaded on or connected to the sheet surface with a size of about 20−50 nm. In Figure 3d, there are no obvious lattice fringes in the high-resolution TEM (HRTEM) image. It indicates that the Fe−Ni particles are amorphous. Because the sample being synthesized by the liquid phase usually lends to a low degree of crystallinity or amorphous.

EDS is used to analyze the elemental information of the sample. The data for samples 2 and 5 are given in Figures S3 and 3b for comparison. Because nitrogen protection is not used in the whole synthesis process, metallic particles can be inevitably partially oxidized, leading to the presence of O in the EDS map. For sample 2 (Figure S3), Fe and O element shows a similar distribution, which is different from that of C, suggesting that most of the oxidation is associated with Fe. However, a much uniform distribution of Fe and Ni is observed for sample 5, Figure 3b. The use of a microchip, which has a better mixing effect than traditional stirring, leads to a more uniform distribution of metallic particles on RGO.

Figure 4a shows XRD patterns of samples 2−5. A noteworthy diffraction peak is found at 26.7° for all the samples, which belongs to the (002) diffraction of RGO.[46] The Fe−Ni−B and Fe particles consist of a broad peak in the 2θ range of 40−50° and no crystalline peak is observed, revealing an amorphous structure.[47] The result is consistent with the HRTEM image result. The amorphous structure is expected to enable samples with a higher BET surface area.

FTIR spectra are also tested for all the samples to characterize the RGO, as shown in Figure 4b. For sample 1, the peak at 1495 cm^{-1} shows that the C=C skeletal vibration of the unoxidized graphitic, of which the C=C has not been reduced to C−H. Absorption bands related to the oxygenated

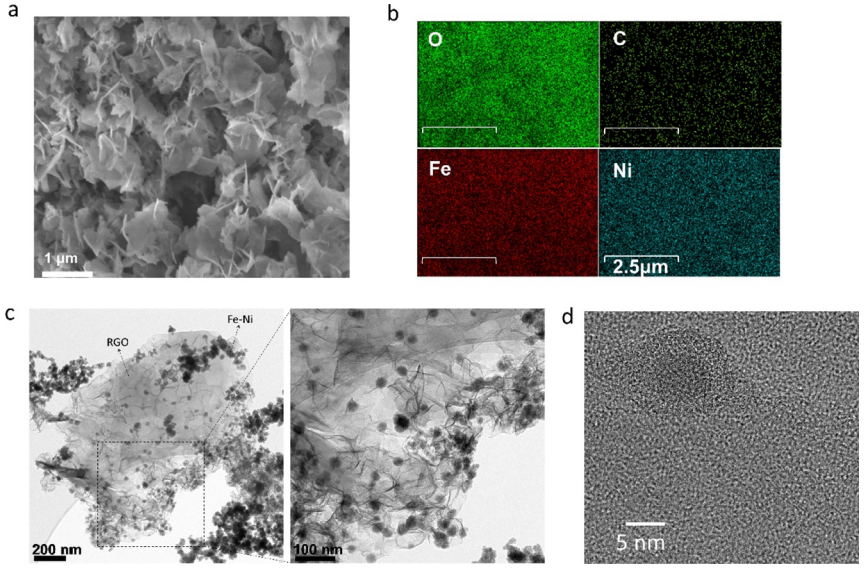

Figure 3. (a) SEM, (b) EDS images, (c) TEM, and (d) HRTEM of Sample 5.

https://doi.org/10.1021/acsomega.1c05273
ACS Omega 2022, 7, 4041−4051

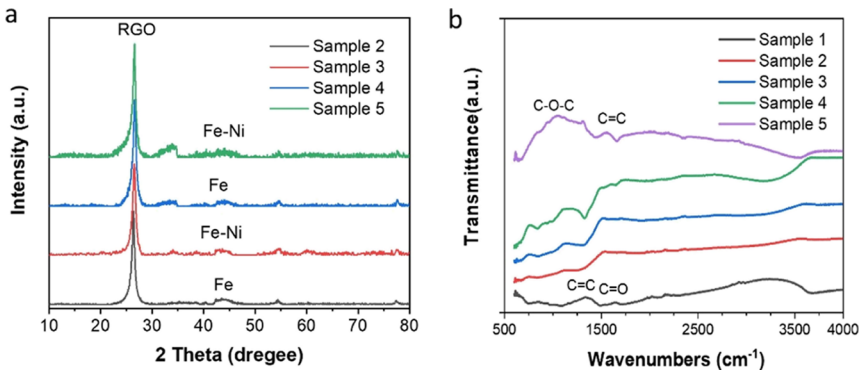

Figure 4. (a) XRD patterns of samples 2−5 and (b) FTIR spectra of samples 1−5.

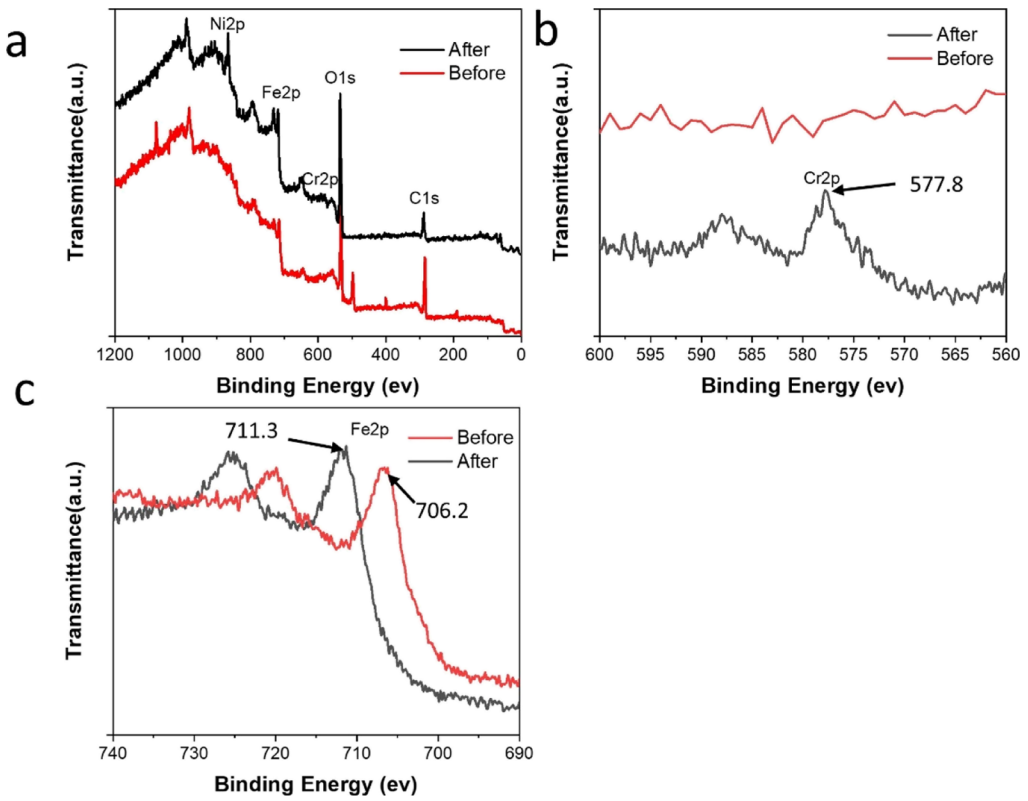

Figure 5. XPS spectra of sample 5 before and after the Cr(VI) adsorption experiment: (a) wide scan, (b) high-resolution spectra of Cr, and (c) high-resolution spectra of Fe.

functional groups dominate the FTIR spectrum. At 1081 cm^{-1}, the alkoxy C−O−C stretching vibration is observed. Peaks at 1705 cm^{-1} belong to the C═O stretching vibration in carbonyl and carboxyl moieties. The O−H stretching vibration in water is at 3673 cm^{-1}. The spectrum shows there are some oxygenated functional groups on it. As there is no surfactant added for sample 1, it may be because that the aggregation of iron and GO prevented the $NaBH_4$ from reducing GO. For samples 2, 3, and 4, there is only a tiny peak, which suggests that nearly all the oxygenated functional groups on GO are reduced. Samples 3 and 4 display a similar result. For sample 5, the O−H stretching vibration in water is at 3538 cm^{-1}. C═C skeletal vibration of the unoxidized graphitic (1654 cm^{-1}) is observed. It means that sample 5 is not entirely reduced, which is due to the reoxidation in the air during the drying or storage process. Compared with sample 1, the disappearance or significant decrease in the intensity of C−O−C, C═C and C═O band in the spectra of samples 2−5 is observed, indicating that the oxygen-containing functional groups in the GO are effectively reduced. However, for all the samples, there are still some oxygen-containing groups on the RGO surface, making the reduced GO slightly negatively charged. As the major Cr(VI) status is $HCrO_4^-$ and $Cr_2O_7^{2-}$, this shall slightly decrease the adsorption capacity due to the electrostatic force.

Figure 5a shows the XPS spectra of sample 5 before and after the Cr(VI) adsorption experiment. The main elements in sample 5 are C, O, Fe, and Ni. After Cr(VI) adsorption experiment, a new peak appeared around 577.8 eV along with the peaks for Cr, as shown in Figure 5b. This pick represents the Cr which exists with Cr(III) hydroxide.[48] This confirmed Cr(VI) is reduced to Cr(III) and adsorbed by the sample. In Figure 5c, before the Cr(VI) adsorption experiment, the peak for Fe is around 706.2 eV, which represents that Fe exists as Fe metal for zero-valent. After Cr(VI) adsorption experiment, the

https://doi.org/10.1021/acsomega.1c05273
ACS Omega 2022, 7, 4041−4051

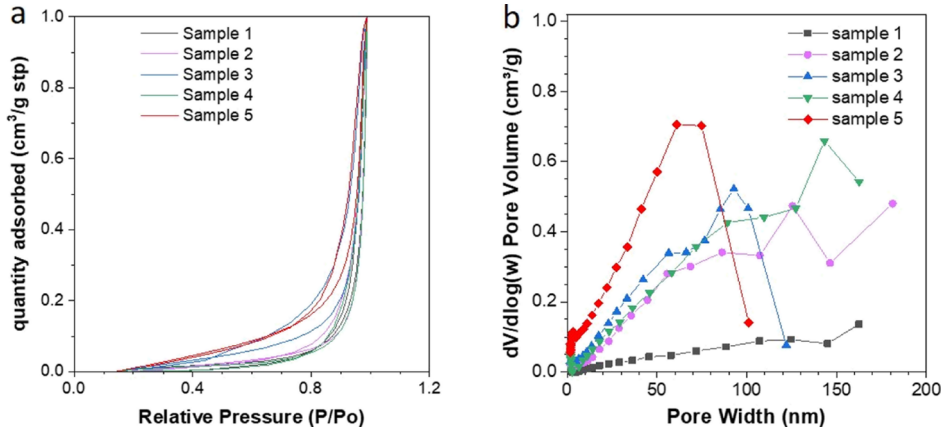

Figure 6. BET results of samples: (a) N_2 adsorption isotherms; (b) pore size distribution data.

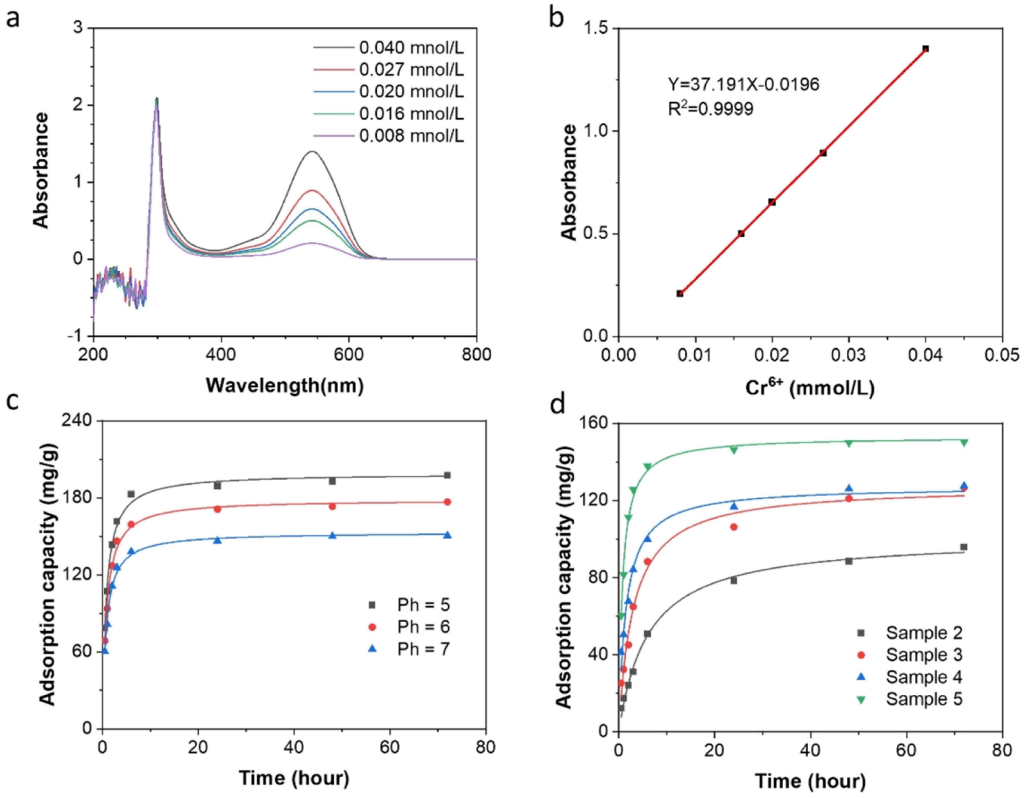

Figure 7. (a) UV−vis spectra of solutions of Cr(VI) reaction with DPC; (b) calibration curve line of Cr(VI) concentration (λ = 545 nm); (c) Cr(VI) adsorption capacity for sample 5 at different pH values; and (d) Cr(VI) adsorption capacity with time and pseudo-second-order kinetic model.

pick left moved to around 711.3 eV, which belongs to Fe_2O_3. This confirmed that Cr(VI) is reduced by NZVI.

3.2. BET Surface Area Study. The specific surface area of all samples is examined by a Micromeritics Tristar 3000. Results are given in Figure 6. The adsorption−desorption isotherm shows that all samples present multilayer adsorption characteristics. The interaction between the adsorbate molecules is stronger than that between the adsorbate and the adsorbent. As the adsorption process progresses, the adsorption appears self-accelerating. The BET specific surface areas of samples 1−5 are calculated as 10.5805, 36.8913, 45.4295, 47.4177, and 119.0778 m^2/g, respectively. Sample 1 is made without any surfactant and showed the lowest BET surface area, which thereby confirmed its low dispersion. With PVP as a surfactant, the BET surface areas of samples 2 and 3 are increased significantly. Though the surfactant can considerably reduce the interfacial tension and improve the separation of particles, there is still some agglomeration of RGO, Fe, and Ni, as confirmed by the zeta sizer results. Such agglomeration may hinder the further increase of the surface area. Comparing samples 2 and 4 with samples 3 and 5, the key factor that affects their surface area is the presence of nickel powder. Nickel powder increases the composite's BET surface area originating from its own high BET surface area and combines with Fe to reduce the possible aggregation of Fe. Meanwhile, samples with nickel powder added have smaller pore width distribution. Sample 5 is dispersed by the microchip, where GO is dispersed in solution very well and

https://doi.org/10.1021/acsomega.1c05273
ACS Omega 2022, 7, 4041−4051

thus provides enough points for Fe and Ni to decorate on. It has the highest BET surface area, up to nearly 3 times compared to that produced by magnetic stirring. Combining the FTIR results, sample 5 is much easier to be reoxidized with a very high specific surface area compared to samples 1−4.

3.3. Cr(VI) Adsorption Capacity Analyses. UV−vis spectroscopy is used to determine the Cr(VI) concentration in a solution based on a validated calibration curve. DPC method is used to measure the Cr(VI) concentration. DPC reacts in an acid medium with chromium(VI) ions to give a violet solution, at λ_{max} = 545 nm, the violet solution obtains a characteristic peak. DPC solution is prepared in advance: 0.2 g of DPC is dissolved in 100 mL of acetone which contains 1 mL of 95% H_2SO_4(1 + 1).

The calibration curve is obtained by measuring a series of concentrations of Cr(VI) solutions reacting with DPC solution. In detail, 23 mL of 0.008, 0.016, 0.020, 0.027, and 0.040 mmol/L Cr(VI) solutions are prepared and, respectively, react with 2 mL of DPC solution. Then, the UV−vis absorption is examined after 5 min at λ_{max} = 545 nm. A linear relationship is shown in Figure 7b for Cr(VI) concentration. That is, $y = 37.191x - 0.0916$ with $R^2 = 0.9999$, where y stands for absorption and x is the Cr(VI) concentration.

20 mg of each sample is added into 40 mL of 2 mmol/L Cr(VI) solution with mechanical oscillation. 0.5 mL of solution is drawn every time at the scheduled time and added into a bottle which includes 2 mL of DPC solution and adds water to 25 mL. After 5 min, The UV absorption spectra of the solution are recorded to determine the remaining Cr(VI) concentration. In most of the cases, the absorption became stable after 72 h (Table 3). In the beginning, all Cr species are in the hexavalent form, the adsorption capacity can be calculated by analyzing the remaining Cr(VI) concentration. After 9 months, the Cr(VI) concentration still kept stable, as shown in Table 3.

Table 3. Cr(VI) Concentration of Samples Deduced for 72 h

	pH	adsorption percentage (%)	adsorption capacity (mg/g)
pure iron	7.0	7.99	16.62
sample 1	7.0	10.67	22.19
sample 2	7.0	46.07	95.83
sample 3	7.0	60.89	126.65
sample 4	7.0	61.33	127.56
sample 5	7.0	72.33	150.45
sample 5	6.0	84.97	176.74
sample 5	5.0	94.92	197.43

It is evident that Fe decorated on RGO has a much higher adsorption capacity than pure NZVI. That is due to the great adsorption ability of RGO. Cr(VI) is adsorbed to the RGO surface, where Cr(VI) can be more efficiently reduced locally by the decorated nano iron. By comparing the results of samples 2 and 4 with samples 3 and 5, it is clear that the addition of a small amount of Ni can naturally increase the adsorption capacity for Cr(VI). This is attributed to the high catalytic performance of Ni particles, which reduces the activation energy needed for the Cr(VI) reduction. The use of the micromixer chip also increases the reduction efficiency greatly as such a device can uniformly mix GO, Fe, and Ni. Sample 5 shows the highest adsorption capacity due to the combined effects of catalytic reaction and good mixing ability of the micromixer chip.

The pH is a key factor affecting Cr(VI) adsorption. In practice, wastewater has a pH ranging from 5 to 8. To reveal the pH affection on Cr(VI) adsorption, Cr(VI) adsorption experiment for sample 5 is tested at pH = 5, 6, and 7. Results are shown in Figure 7c. Consistent with previous studies, lower pH is a benefit for Cr(VI) adsorption. A higher reaction rate and adsorption capacity are realized in lower pH.

The reusability and stability of samples are also investigated. The used samples are collected from the solution by filtration, dispersed in water, and added excess $NaBH_4$ to reduce Fe_2O_3 to ZVI. Then, after filtration and drying, the Cr(VI) adsorption capacity for used samples under the same condition as new samples is analyzed. Results are shown in Table 4. The low adsorption percentage and adsorption capacity indicated that the reused samples nearly totally lost the Cr(VI) reduction ability. Because the Cr(III) hydroxide is absorbed by Fe−Ni/RGO after the first time adsorption, all possible reduction points have been occupied by Cr(III) hydroxide which is stable under $NaBH_4$ and difficult to disperse back to the solution. Though strong acid or strong base can simply dissolve Cr(III) hydroxide from Fe−Ni/RGO, it could also destroy the components of Fe−Ni/RGO. Hence, the samples cannot be reused easily, but keep the possibility. Future research will be carried out to improve the property of reusability.

Table 4. Sample Reusability and Stability for Cr(VI) Adsorption

	sample 2	sample 3	sample 4	sample 5
Adsorption Percentage For pH = 7.0				
new sample	46.07%	60.89%	61.33%	72.33%
reused sample	2.78%	3.86%	3.32%	4.31%
after 9 months	45.85%	60.54%	61.25%	72.10%
Adsorption Capacity (mg/g) For pH = 7.0				
new sample	95.83	126.65	127.56	150.45
reused sample	5.79	8.02	6.91	8.96
after 9 months	95.36	125.92	127.39	149.97

To verification the stability of samples, let samples stand in the reaction solution for 9 months after the Cr(VI) adsorption experiment and then characterized the Cr(VI) concentration in solution. Results are shown in Table 4. The Cr(VI) adsorption percentage and adsorption capacity keeps stable after 9 months. This is due to that the generated Cr(III) hydroxide being absorbed by Fe−Ni/RGO is stable and difficult to disperse back to the solution.

Table 5 shows a comparison of the Cr(VI) adsorption capacity with NZVI-based materials reported in the literature. As the initial concentration of Cr(VI), the ratio between Cr(VI) and reductant can vary in the literature. The best way to evaluate the material is adsorption capacity (mg/g) under a similar pH. In practice, wastewater has a pH ranging from 5 to 8. Considering this fact, the proposed particles (sample 5) in our study present the highest adsorption capacity, benefiting from their extremely high BET surface area and uniform distribution of Ni and Fe NPs on the RGO surface.

To reveal the Cr(VI) adsorption kinetics of samples 2−5, adsorption capacity is characterized with different times, as shown in Figure 7d. The adsorption is initially fast because of lots of sites available at first, and then, the adsorption speed

https://doi.org/10.1021/acsomega.1c05273
ACS Omega 2022, 7, 4041−4051

Table 5. Cr(VI) Adsorption Capacity Reported by the Literature

raw material	pH	adsorption capacity (mg/g)	references
NZVI	5.0	47.2	21
NZVI	6.0	62.4	49
NZVI	5.5	66.7	27
NZVI/rGO	4.25	162	40
NZVI/rGO	5.0	180.64	41
NZVI/rGO	7.0	21.72	42
Fe_2O_3/graphene	8	66.2	43
Fe−Ni/RGO	7.0	150.45	this work
Fe−Ni/RGO	6.0	176.74	this work
Fe−Ni/RGO	5.0	197.43	this work

slows down with prolonging the time and reaches equilibrium after 72 h.

The results are researched by the pseudo-first-order kinetic model and pseudo-second-order kinetic model.

A linear form of the pseudo-first-order kinetic model is given as

$$\log(q_e - q_t) = \log\ q_e - K_1 t$$

A linear form of the pseudo-second-order kinetic model is given as

$$\frac{t}{q_t} = \frac{1}{K_2 q_e^2} + \frac{t}{q_e}$$

where q_e and q_t (mg/g) are the adsorption capacity of Cr(VI) at equilibrium and t time (hour). K_1 (g/mg/h) and K_2 (g/mg/h) are pseudo-first-order kinetic model and pseudo-second-order kinetic model rate constants, respectively.

Table 6 shows the analysis results for the pseudo-first-order kinetic model and pseudo-second-order kinetic model.

Table 6. Pseudo-First-Order Kinetic Model and Pseudo-Second-Order Kinetic Model Results

	sample 2	sample 3	sample 4	sample 5
Pseudo-First-Order Kinetic Model				
q_e (mg/g)	88.6785	117.3945	119.8971	144.8995
K_1 (g/mg/h)	0.0640	0.1143	0.1956	0.3555
R^2-adjusted	0.9731	0.9591	0.9086	0.9559
Pseudo-Second-Order Kinetic Model				
q_e (mg/g)	100.9509	127.56231	127.30039	153.17131
K_2 (g/mg/h)	0.0016	0.0026	0.0052	0.0084
R^2-adjusted	0.9923	0.9828	0.9790	0.9926

Compared with the pseudo-first-order kinetic model, the pseudo-second-order kinetic model got adjusted R^2 more close to 1, which means that the pseudo-second-order kinetic model is more suitable for the samples. This confirmed that the adsorption process is not physical adsorption, but chemical adsorption.

3.4. Cr(VI) Reduce Reaction Mechanism and Kinetic Model. The large capacity of the new materials can be attributed to several reasons. First, the RGO is synthesized by the GO reduction method, and it is unavoidable that there is a small amount of the oxygen-containing functional group left on RGO. The oxygen-containing functional group can provide anchor points for Fe and Ni NPs and limit the excessive growth of the NPs,[50] which thereby increase the dispersion and stability of Fe and Ni. Second, the located Fe and Ni NPs can prevent the aggregation of RGO via the increase of the surface spacing of RGO. Third, RGO has an extremely high specific surface area and a strong adsorption capacity for Cr(VI). Once Cr(VI) is adsorbed on the RGO surface, the nanoscale ZVI will transport electrons to Cr(VI) to reduce it to Cr(III). For the Ni−Fe bimetal, nickel powder acts as a catalyzer for the redox reaction between ZVI and Cr(VI).

Schematically, the process is illustrated in Figure 8. The main reaction route for NZVI reducing Cr(VI) is the electron transfer from Fe^0 ($E^0_{Fe^{2+}/Fe^0} = -0.44$ V) to Cr(VI) ($E^0_{HCrO_4^-/Cr^{3+}} = 1.36$ V)[51]

$$2HCrO_4^- + 14H^+ + 3Fe^0(s) \rightarrow 2Cr^{3+} + 8H_2O + 3Fe^{2+}$$

As $E^0_{Fe^{3+}/Fe^{2+}} = 0.77\ \text{V} < E^0_{HCrO_4^-/Cr^{3+}}$, the generated Fe^{2+} will also react with Cr(VI)[52]

$$HCrO_4^- + 7H^+ + 3Fe^{2+} \rightarrow Cr(III) + 4H_2O + 3Fe^{3+}$$

The electrons also transfer from Fe^0 to Fe^{3+}

$$Fe^0 + 2Fe^{3+} \rightarrow 3Fe^{2+}$$

After adding Ni, due to the catalytic action, the reaction activity of Fe^0 will be much higher than that without Ni.[53,54] The reaction mechanism is shown below:

$$Fe^0 + 2H_2O \rightarrow Fe^{2+} + H_2 + 2OH^-$$

$$2Ni^0 + H_2 \rightarrow 2Ni^0 - H^\bullet$$

$$HCrO_4^- + 3Ni^0 - H^\bullet + 4H^+ \rightarrow Cr(III) + 4H_2O + 3Ni^0$$

At this stage, XPS results indicate that the Cr(III) will form insoluble Cr(III) hydroxide and be absorbed by Fe−Ni/RGO. The absorption is stable and Cr(III) will not be dissolved back in the solution for a long time. The absorbed Cr(III) hydroxide will occupy some surface area of Fe−Ni/RGO and lead a decrease of reaction rate. Meanwhile, the Cr(III) hydroxide could cover up some unreacted ZVI to reduce the final adsorption capacity.

At low pH, the major Cr(VI) status is $HCrO_4^-$ and $Cr_2O_7^{2-}$.[18] The higher removal efficiency at low pH is attributed to that the surface of the adsorbent becomes highly protonated and positively charged. The adsorbent can attract $HCrO_4^-$ and $Cr_2O_7^{2-}$ via electrostatic force. With the increase of pH, less H^+ and more OH^- hugely affected the reaction rate and equilibrium. Also, the adsorbent's surface will be negatively charged, which then highly decreases the adsorption capacity.

The following results are considered:

- All electrons are moved initially from Fe species and finally got by Cr species, it can be considered as Fe is the only element capable of reducing Cr(VI)
- The equation rate for the Cr(VI) reduction is first-order.
- The conversion ratio between Cr(VI) and Cr(III) is 1:1.

Considering the reaction mechanism mentioned above, a kinetic model is proposed to describe the Cr(VI) removal; when the pH and temperature are constant, the rate of Cr(VI) reduction by samples can be found as

$$\frac{d[Cr(VI)]}{dt} = -k[SC][Cr(VI)]$$

where [Cr(VI)] is the hexavalent chromium concentration (mmol/L) at time t and k is its rate coefficient (L mmol^{-1}

https://doi.org/10.1021/acsomega.1c05273
ACS Omega 2022, 7, 4041−4051

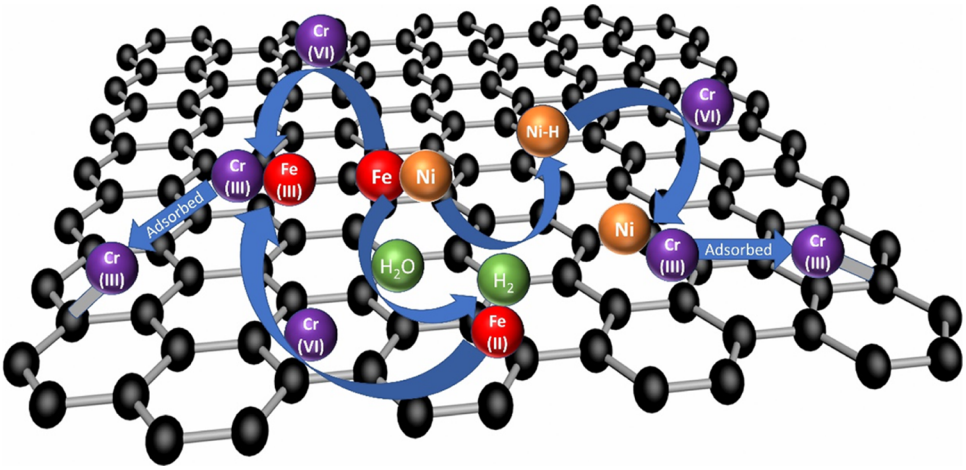

Figure 8. Cr(VI) adsorption and reduction mechanism of samples with RGO.

h^{-1}), and [SC] represents the equivalent sample concentration at time t capable of reducing Cr(VI) (mmol L^{-1}).

Considering that Fe^0 is oxidized during Cr(VI) reduction, the equivalent sample concentration on the surface of the samples decreases during the reaction and can be calculated as

$$[SC]_t = C^*_{SC}[S]\left(1 - \frac{[Cr(VI)]_0 - [Cr(VI)]_t}{C^*_{SC}[S]}\right)$$

where C^*_{SC} is the removal capacity of Cr(VI) per unit gram of sample (mmol/g), which is obtained by the adsorption capacity analysis experiment. [S] is the sample concentration (g/L), and $C^*_{SC}[S]$, represents the initial concentration of [SC]. $[Cr(VI)]_0$ is the initial hexavalent chromium concentration (mmol/L). $\frac{[Cr(VI)]_0 - [Cr(VI)]_t}{C^*_{SC}[S]}$ represents the fraction of [SC] oxidized.

Integrate the above eqs, results in

$$[Cr(VI)]_t = \frac{[Cr(VI)]_0\{C^*_{SC}[S] - [Cr(VI)]_0\}}{C^*_{SC}[S]\ \exp\{k(C^*_{SC}[S] - [Cr(VI)]_0 t)\} - [Cr(VI)]_0}$$

where k and C^*_{SC} are the model constant parameters and t is the reaction time (hour). The fitting result of the kinetic model is shown below (Table 7 and Figure 9):

Table 7. The Kinetic Model Results

	sample 2	sample 3	sample 4	sample 5
K (h^{-1})	0.0798	0.1563	0.2807	0.5549
C^*_{SC} (mmol/g)	1.7392	2.2914	2.3445	2.8483
R^2-adjusted	0.9822	0.9710	0.9507	0.9928

The results show that the kinetic model has high adjusted R^2, which confirmed that the reaction mechanism and model are reasonable for the reduction reaction. By comparing the rate coefficient k between samples 2, 4 and samples 3, 5, it indicated the added Ni nearly doubled the rate coefficient for both with and without microchip samples, which is due to the catalyst effect of Ni. Also, from the model results, it indicated that after microchip mixture and dispersion, the rate coefficient k can get hugely increased. Combine with the above morphology analyses, that is because the microchip gives the sample more contact area among Fe, Ni, and Cr(VI).

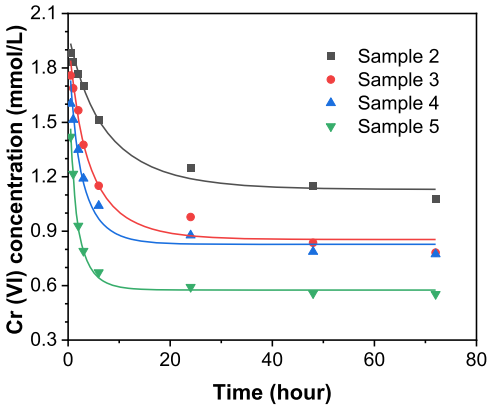

Figure 9. Kinetic model curve for samples 2−5.

4. CONCLUSIONS

In summary, we constructed a novel Ni−Fe/RGO composite for the effective removal of Cr(VI) in an aqueous solution, where RGO acts as an adsorbent, Ni as the catalysis, and Fe as the reducing agent. Intensifying the mixing through a microchip leads to an improved dispersion and further enhanced Cr(VI) adsorption capacity.

- The added Ni nearly doubled the BET surface area compared with samples without Ni. This is due to its own high BET surface area and its combination with Fe NPs reduces the possible aggregation of Fe NPs. The Cr(VI) adsorption capacity and rate coefficient are enhanced with the catalyzation of Ni and higher BET surface area.
- The Ni−Fe/RGO composite exhibits the highest Cr(VI) adsorption capacity of 150.45 mg/g at pH = 7 and 197.43 mg/g at pH = 5. RGO supplied a mass of sites for Fe and Ni NPs to load on, which promotes the dispersion of Fe and Ni NPs and prevents their aggregation. Meanwhile, the loaded Fe and Ni NPs also prevent the aggregation of RGO due to the increased surface spacing of RGO. The synergistic effects enable the sample with a high BET surface area

https://doi.org/10.1021/acsomega.1c05273
ACS Omega 2022, 7, 4041−4051

and Cr(VI) adsorption capacity. The adsorption process fits the pseudo-second-order kinetic model.

- The microchip presents a better dispersal ability of GO in solution than traditional magnetic stirring and thereby could avoid the agglomeration of GO. Samples are demonstrated with enough points to load the Fe−Ni bimetal, resulting in a much higher Cr(VI) adsorption capacity and rate coefficient.
- Meanwhile, the materials are synthesized by a convenient and cheap method without nitrogen protection compared with other reports.

■ ASSOCIATED CONTENT

Supporting Information

The Supporting Information is available free of charge at https://pubs.acs.org/doi/10.1021/acsomega.1c05273.

Schematic micromixer chip; UV−vis absorption spectra of solutions with different Cr(III) concentrations; image of solutions mixed by microchip and magnetic stirring method; and EDS data of sample 2 (PDF)

■ AUTHOR INFORMATION

Corresponding Authors

Hui Gao − *School of Aeronautic Science and Engineering, Beihang University, 100191 Beijing, P. R. China;* orcid.org/0000-0002-0220-6411; Email: h.gao@buaa.edu.cn

Dongsheng Wen − *School of Chemical and Process Engineering, University of Leeds, Leeds LS2 9JT, U.K.; School of Aeronautic Science and Engineering, Beihang University, 100191 Beijing, P. R. China;* orcid.org/0000-0003-3492-7982; Email: d.wen@leeds.ac.uk, d.wen@buaa.edu.cn

Authors

Zeyu Kang − *School of Chemical and Process Engineering, University of Leeds, Leeds LS2 9JT, U.K.*

Zhongliang Hu − *School of Chemical and Process Engineering, University of Leeds, Leeds LS2 9JT, U.K.*

Xiaodong Jia − *School of Chemical and Process Engineering, University of Leeds, Leeds LS2 9JT, U.K.*

Complete contact information is available at: https://pubs.acs.org/10.1021/acsomega.1c05273

Author Contributions

The manuscript was written through the contributions of all authors. All authors have given approval to the final version of the manuscript.

Notes

The authors declare no competing financial interest.

■ ACKNOWLEDGMENTS

Thanks to the financial support from the University of Leeds for the research.

■ REFERENCES

(1) Miensah, E. D.; Khan, M. M.; Chen, J. Y.; Zhang, X. M.; Wang, P.; Zhang, Z. X.; Jiao, Y.; Liu, Y.; Yang, Y. Zeolitic imidazolate frameworks and their derived materials for sequestration of radionuclides in the environment: A review. *Crit. Rev. Environ. Sci. Technol.* **2020**, *50*, 1874−1934.

(2) Tang, J.; Zhang, J.; Ren, L.; Zhou, Y.; Gao, J.; Luo, L.; Yang, Y.; Peng, Q.; Huang, H.; Chen, A. Diagnosis of soil contamination using microbiological indices: A review on heavy metal pollution. *J. Environ. Manage.* **2019**, *242*, 121−130.

(3) He, J.; Yang, Y.; Christakos, G.; Liu, Y.; Yang, X. Assessment of soil heavy metal pollution using stochastic site indicators. *Geoderma* **2019**, *337*, 359−367.

(4) Shen, H.; Chen, J.; Dai, H.; Wang, L.; Hu, M.; Xia, Q. New Insights into the Sorption and Detoxification of Chromium(VI) by Tetraethylenepentamine Functionalized Nanosized Magnetic Polymer Adsorbents: Mechanism and pH Effect. *Ind. Eng. Chem. Res.* **2013**, *52*, 12723−12732.

(5) Zhao, Y.; Zhao, D.; Chen, C.; Wang, X. Enhanced photo-reduction and removal of Cr(VI) on reduced graphene oxide decorated with TiO2 nanoparticles. *J. Colloid Interface Sci.* **2013**, *405*, 211−217.

(6) Ku, Y.; Jung, I.-L. Photocatalytic reduction of Cr(VI) in aqueous solutions by UV irradiation with the presence of titanium dioxide. *Water Res.* **2001**, *35*, 135−142.

(7) Kang, S.-Y.; Lee, J.-U.; Moon, S.-H.; Kim, K.-W. Competitive adsorption characteristics of Co2+, Ni2+, and Cr3+ by IRN-77 cation exchange resin in synthesized wastewater. *Chemosphere* **2004**, *56*, 141−147.

(8) Polat, H.; Erdogan, D. Heavy metal removal from waste waters by ion flotation. *J. Hazard. Mater.* **2007**, *148*, 267−273.

(9) Ölmez, T. The optimization of Cr(VI) reduction and removal by electrocoagulation using response surface methodology. *J. Hazard. Mater.* **2009**, *162*, 1371−1378.

(10) Fu, F.; Wang, Q. Removal of heavy metal ions from wastewaters: A review. *J. Environ. Manage.* **2011**, *92*, 407−418.

(11) Gould, J. P. The kinetics of hexavalent chromium reduction by metallic iron. *Water Res.* **1982**, *16*, 871−877.

(12) Blowes, D.; Ptacek, C. Geochemical remediation of groundwater by permeable reactive walls: removal of chromate by reaction with iron-bearing solids. *Subsurface Restoration Conference; 3rd International Conference on Ground Water Quality Research*,June, 1992; pp 21−24.

(13) Chang, L.-Y. Alternative chromium reduction and heavy metal precipitation methods for industrial wastewater. *Environ. Prog.* **2003**, *22*, 174−182.

(14) Blowes, D. W.; Ptacek, C. J.; Jambor, J. L. In-Situ Remediation of Cr(VI)-Contaminated Groundwater Using Permeable Reactive Walls: Laboratory Studies. *Environ. Sci. Technol.* **1997**, *31*, 3348−3357.

(15) Ramos, M. A. V.; Yan, W.; Li, X.-q.; Koel, B. E.; Zhang, W.-x. Simultaneous Oxidation and Reduction of Arsenic by Zero-Valent Iron Nanoparticles: Understanding the Significance of the Core−Shell Structure. *J. Phys. Chem. C* **2009**, *113*, 14591−14594.

(16) Boparai, H. K.; Joseph, M.; O'Carroll, D. M. Kinetics and thermodynamics of cadmium ion removal by adsorption onto nano zerovalent iron particles. *J. Hazard. Mater.* **2011**, *186*, 458−465.

(17) Hwang, Y.-H.; Kim, D.-G.; Shin, H.-S. Mechanism study of nitrate reduction by nano zero valent iron. *J. Hazard. Mater.* **2011**, *185*, 1513−1521.

(18) García-Sosa, I.; Olguín, M. T. Comparison Between the Cr(VI) Adsorption by Hydrotalcite and Hydrotalcite-Gibbsite Compounds. *Sep. Sci. Technol.* **2015**, *50*, 2631−2638.

(19) Jung, C.; Heo, J.; Han, J.; Her, N.; Lee, S.-J.; Oh, J.; Ryu, J.; Yoon, Y. Hexavalent chromium removal by various adsorbents: Powdered activated carbon, chitosan, and single/multi-walled carbon nanotubes. *Sep. Purif. Technol.* **2013**, *106*, 63−71.

(20) Cao, J.; Zhang, W.-X. Stabilization of chromium ore processing residue (COPR) with nanoscale iron particles. *J. Hazard. Mater.* **2006**, *132*, 213−219.

(21) Montesinos, V. N.; Quici, N.; Beatriz Halac, E.; Leyva, A. G.; Custo, G.; Bengio, S.; Zampieri, G.; Litter, M. I. Highly efficient removal of Cr(VI) from water with nanoparticulated zerovalent iron: Understanding the Fe(III)-Cr(III) passive outer layer structure. *Chem. Eng. J.* **2014**, *244*, 569−575.

(22) Chen, Z.; Wei, D.; Li, Q.; Wang, X.; Yu, S.; Liu, L.; Liu, B.; Xie, S.; Wang, J.; Chen, D.; Hayat, T.; Wang, X. Macroscopic and

microscopic investigation of Cr(VI) immobilization by nanoscaled zero-valent iron supported zeolite MCM-41 via batch, visual, XPS and EXAFS techniques. *J. Cleaner Prod.* **2018**, *181*, 745−752.
(23) Ai, Z.; Cheng, Y.; Zhang, L.; Qiu, J. Efficient Removal of Cr(VI) from Aqueous Solution with Fe@Fe2O3 Core−Shell Nanowires. *Environ. Sci. Technol.* **2008**, *42*, 6955−6960.
(24) Lv, Z.; Yang, S.; Chen, L.; Alsaedi, A.; Hayat, T.; Chen, C. Nanoscale zero-valent iron/magnetite carbon composites for highly efficient immobilization of U(VI). *J. Environ. Sci.* **2019**, *76*, 377−387.
(25) O'Carroll, D.; Sleep, B.; Krol, M.; Boparai, H.; Kocur, C. Nanoscale zero valent iron and bimetallic particles for contaminated site remediation. *Adv. Water Resour.* **2013**, *51*, 104−122.
(26) Yu, S.; Pang, H.; Huang, S.; Tang, H.; Wang, S.; Qiu, M.; Chen, Z.; Yang, H.; Song, G.; Fu, D.; Hu, B.; Wang, X. Recent advances in metal-organic framework membranes for water treatment: A review. *Sci. Total Environ.* **2021**, *800*, 149662.
(27) Zhou, X.; Lv, B.; Zhou, Z.; Li, W.; Jing, G. Evaluation of highly active nanoscale zero-valent iron coupled with ultrasound for chromium(VI) removal. *Chem. Eng. J.* **2015**, *281*, 155−163.
(28) Lv, X.; Xu, J.; Jiang, G.; Tang, J.; Xu, X. Highly active nanoscale zero-valent iron (nZVI)-Fe3O4 nanocomposites for the removal of chromium(VI) from aqueous solutions. *J. Colloid Interface Sci.* **2012**, *369*, 460−469.
(29) Huang, Q.; Liu, W.; Peng, P. a.; Huang, W. Reductive dechlorination of tetrachlorobisphenol A by Pd/Fe bimetallic catalysts. *J. Hazard. Mater.* **2013**, *262*, 634−641.
(30) Lai, B.; Zhang, Y.; Chen, Z.; Yang, P.; Zhou, Y.; Wang, J. Removal of p-nitrophenol (PNP) in aqueous solution by the micron-scale iron-copper (Fe/Cu) bimetallic particles. *Appl. Catal., B* **2014**, *144*, 816−830.
(31) Chen, B.; Zhu, Z.; Hong, J.; Wen, Z.; Ma, J.; Qiu, Y.; Chen, J. Nanocasted synthesis of ordered mesoporous cerium iron mixed oxide and its excellent performances for As(v) and Cr(vi) removal from aqueous solutions. *Dalton Trans.* **2014**, *43*, 10767−10777.
(32) Wen, Z.; Zhang, Y.; Cheng, G.; Wang, Y.; Chen, R. Simultaneous removal of As(V)/Cr(VI) and acid orange 7 (AO7) by nanosized ordered magnetic mesoporous Fe-Ce bimetal oxides: Behavior and mechanism. *Chemosphere* **2019**, *218*, 1002−1013.
(33) Zhou, X.; Jing, G.; Lv, B.; Zhou, Z.; Zhu, R. Highly efficient removal of chromium(VI) by Fe/Ni bimetallic nanoparticles in an ultrasound-assisted system. *Chemosphere* **2016**, *160*, 332−341.
(34) Shi, L.-n.; Zhang, X.; Chen, Z.-l. Removal of Chromium (VI) from wastewater using bentonite-supported nanoscale zero-valent iron. *Water Res.* **2011**, *45*, 886−892.
(35) Fu, R.; Yang, Y.; Xu, Z.; Zhang, X.; Guo, X.; Bi, D. The removal of chromium (VI) and lead (II) from groundwater using sepiolite-supported nanoscale zero-valent iron (S-NZVI). *Chemosphere* **2015**, *138*, 726−734.
(36) Wang, Q.; Qian, H.; Yang, Y.; Zhang, Z.; Naman, C.; Xu, X. Reduction of hexavalent chromium by carboxymethyl cellulose-stabilized zero-valent iron nanoparticles. *J. Contam. Hydrol.* **2010**, *114*, 35−42.
(37) Sharma, A. K.; Kumar, R.; Mittal, S.; Hussain, S.; Arora, M.; Sharma, R. C.; Babu, J. N. In situ reductive regeneration of zerovalent iron nanoparticles immobilized on cellulose for atom efficient Cr(vi) adsorption. *RSC Adv.* **2015**, *5*, 89441−89446.
(38) O'Carroll, D.; Sleep, B.; Krol, M.; Boparai, H.; Kocur, C. Nanoscale zero valent iron and bimetallic particles for contaminated site remediation. *Adv. Water Resour.* **2013**, *51*, 104−122.
(39) Tkachev, S. V.; Buslaeva, E. Y.; Naumkin, A. V.; Kotova, S. L.; Laure, I. V.; Gubin, S. P. Reduced graphene oxide. *Inorg. Mater.* **2012**, *48*, 796−802.
(40) Jabeen, H.; Chandra, V.; Jung, S.; Lee, J. W.; Kim, K. S.; Kim, S. B. Enhanced Cr(vi) removal using iron nanoparticle decorated graphene. *Nanoscale* **2011**, *3*, 3583−3585.
(41) Li, J.; Chen, C.; Zhang, R.; Wang, X. Nanoscale Zero-Valent Iron Particles Supported on Reduced Graphene Oxides by Using a Plasma Technique and Their Application for Removal of Heavy-Metal Ions. *Chem.—Asian J.* **2015**, *10*, 1410−1417.
(42) Li, X.; Ai, L.; Jiang, J. Nanoscale zerovalent iron decorated on graphene nanosheets for Cr(VI) removal from aqueous solution: Surface corrosion retard induced the enhanced performance. *Chem. Eng. J.* **2016**, *288*, 789−797.
(43) Lv, X.; Xue, X.; Jiang, G.; Wu, D.; Sheng, T.; Zhou, H.; Xu, X. Nanoscale Zero-Valent Iron (nZVI) assembled on magnetic Fe3O4/graphene for Chromium (VI) removal from aqueous solution. *J. Colloid Interface Sci.* **2014**, *417*, 51−59.
(44) Wang, D.; Zhang, G.; Zhou, L.; Wang, M.; Cai, D.; Wu, Z. Synthesis of a Multifunctional Graphene Oxide-Based Magnetic Nanocomposite for Efficient Removal of Cr(VI). *Langmuir* **2017**, *33*, 7007−7014.
(45) Lu, H.; Tian, B.; Wang, J.; Hao, H. Montmorillonite-Supported Fe/Ni Bimetallic Nanoparticles for Removal of Cr (VI) from Wastewater. *Chem. Eng. Trans.* **2017**, *60*, 169−174.
(46) Saleem, H.; Haneef, M.; Abbasi, H. Y. Synthesis route of reduced graphene oxide via thermal reduction of chemically exfoliated graphene oxide. *Mater. Chem. Phys.* **2018**, *204*, 1−7.
(47) Yang, C.; Yu, M.; Zhao, S.; Tian, Y.; Bian, X. Magnetoviscous Property and Hyperthermia Effect of Amorphous Nanoparticle Aqueous Ferrofluids. *Nanoscale Res. Lett.* **2018**, *13*, 378.
(48) Biesinger, M. C.; Payne, B. P.; Grosvenor, A. P.; Lau, L. W. M.; Gerson, A. R.; Smart, R. S. C. Resolving surface chemical states in XPS analysis of first row transition metals, oxides and hydroxides: Cr, Mn, Fe, Co and Ni. *Appl. Surf. Sci.* **2011**, *257*, 2717−2730.
(49) Wang, Q.; Cissoko, N.; Zhou, M.; Xu, X. Effects and mechanism of humic acid on chromium(VI) removal by zero-valent iron (Fe0) nanoparticles. *Phys. Chem. Earth, Part A/B/C* **2011**, *36*, 442−446.
(50) Jasuja, K.; Berry, V. Implantation and Growth of Dendritic Gold Nanostructures on Graphene Derivatives: Electrical Property Tailoring and Raman Enhancement. *ACS Nano* **2009**, *3*, 2358−2366.
(51) Gheju, M. Hexavalent Chromium Reduction with Zero-Valent Iron (ZVI) in Aquatic Systems. *Water, Air, Soil Pollut.* **2011**, *222*, 103−148.
(52) dos Santos Coelho, F.; Ardisson, J. D.; Moura, F. C. C.; Lago, R. M.; Murad, E.; Fabris, J. D. Potential application of highly reactive Fe(0)/Fe3O4 composites for the reduction of Cr(VI) environmental contaminants. *Chemosphere* **2008**, *71*, 90−96.
(53) Tee, Y.-H.; Grulke, E.; Bhattacharyya, D. Role of Ni/Fe Nanoparticle Composition on the Degradation of Trichloroethylene from Water. *Ind. Eng. Chem. Res.* **2005**, *44*, 7062−7070.
(54) Schrick, B.; Blough, J. L.; Jones, A. D.; Mallouk, T. E. Hydrodechlorination of Trichloroethylene to Hydrocarbons Using Bimetallic Nickel−Iron Nanoparticles. *Chem. Mater.* **2002**, *14*, 5140−5147.

https://doi.org/10.1021/acsomega.1c05273
ACS Omega 2022, 7, 4041−4051